


Article

Identifying Multi-Scale Gravity and Magnetic Anomalies Using Statistical Empirical Mode Decomposition: A Case Study from the Eastern Tianshan Orogenic Belt

Fan Xiao ^{1,2,3,4,*} , Weipeng Lin ¹, Huaqing Yang ¹ and Cuicui Wang ⁵

¹ School of Earth Sciences and Engineering, Sun Yat-sen University, Zhuhai 519000, China; linwp6@mail2.sysu.edu.cn (W.L.); yanghq36@mail2.sysu.edu.cn (H.Y.)

² Guangdong Provincial Key Laboratory of Geological Process and Mineral Resource Exploration, Sun Yat-sen University, Zhuhai 519000, China

³ Guangdong Provincial Key Laboratory of Geodynamics and Geohazards, Sun Yat-sen University, Zhuhai 519000, China

⁴ Southern Marine Science and Engineering Guangdong Laboratory (Zhuhai), Zhuhai 519000, China

⁵ Urumqi Comprehensive Survey Center on Natural Resources, China Geological Survey, Urumqi 830026, China; wcc7011@hotmail.com

* Correspondence: xiaofan3@mail.sysu.edu.cn; Tel./Fax: +86-020-84112390

Abstract: Identifying multi-scale anomalies that have simple forms and geological significance is critical for enhancing the interpretability of gravity and magnetic survey data. In recent years, empirical mode decomposition (EMD), which was developed as a significant data-driven approach for analyzing complex signals, has been widely used in identifying gravity and magnetic anomalies due to its advantages of adaptability to nonlinear and nonstationary data. Nevertheless, the traditional EMD method is usually sensitive to outliers and irregularly spaced data because of the interpolation process in the construction of envelopes. In this regard, an extended algorithm called statistical EMD (SEMD) has been proposed based on the smoothing technique. In this study, for validation purposes, the novel SEMD method has been employed to identify multi-scale gravity and magnetic anomalies. The sensitivities of local polynomial and cubic spline smoothing methods in SEMD to combination and arrangement patterns of field sources including the size, depth, and distance in gravity and magnetic anomaly identification were investigated and compared by forward modeling under the same conditions. The results demonstrated that the local polynomial smoothing method performed better than the cubic spline smoothing method. Thus, in the case study, the SEMD method using the local polynomial smoothing technique was employed for identifying multi-scale gravity and magnetic anomalies in the eastern Tianshan orogenic belt, northwestern China. It has illustrated that the SEMD method provides a novel and useful data-driven method for extracting gravity and magnetic anomalies.

Keywords: empirical mode decomposition; Bouguer gravity; aerial magnetic; intrinsic mode function; eastern Tianshan; China



Citation: Xiao, F.; Lin, W.; Yang, H.; Wang, C. Identifying Multi-Scale Gravity and Magnetic Anomalies Using Statistical Empirical Mode Decomposition: A Case Study from the Eastern Tianshan Orogenic Belt. *Minerals* **2023**, *13*, 1118. <https://doi.org/10.3390/min13091118>

Academic Editors: Emilio L. Pueyo, Yongqing Chen, Xianchuan Yu and Jiangnan Zhao

Received: 15 June 2023

Revised: 18 August 2023

Accepted: 22 August 2023

Published: 24 August 2023



Copyright: © 2023 by the authors. Licensee MDPI, Basel, Switzerland. This article is an open access article distributed under the terms and conditions of the Creative Commons Attribution (CC BY) license (<https://creativecommons.org/licenses/by/4.0/>).

1. Introduction

Identifying significant anomalies with simple forms and geological meanings is one of the most fundamental tasks for interpreting gravity and magnetic survey data [1–3]. Nevertheless, it is usually hindered by nonlinear and nonstationary gravity and magnetic data, which are superimposed by complex signals from multiple field sources that may have different sizes or/and may be located at different depths [4]. Thus, in the past several decades, many sophisticated signal processing methods such as spectral analysis [5,6], wavelet analysis [7,8], fractal analysis [9–11], singular value decomposition [8,12–16], and empirical mode decomposition (EMD) [17] have been employed to extract gravity and magnetic anomalies. In these methods, EMD has been increasingly applied as a data-driven

approach for decomposing complex gravity and magnetic signals due to its strong adaptability to nonlinear and nonstationary data. This is because it defines and utilizes intrinsic mode functions (IMFs) to isolate a given signal according to the local oscillation magnitude in the physical domain [18–25]. For instance, Huang et al. [26] used the bidimensional EMD (BEMD) method to handle the gravity data of a gold field, which yielded IMF maps depicting the spatial distribution relationship between gold deposits and the geological units; Chen et al. [27] decomposed gravity and magnetic signals using the BEMD method to extract the local anomalies that indicate exploration targets; Hou et al. [28] applied BEMD to separate the magnetic anomalies associated with silver, lead, and zinc polymetallic deposits from a regional field; Zhao et al. [29] developed an improved BEMD method and used it to characterize the multi-scale anomalies of aeromagnetic survey data; Chen et al. [30] employed BEMD to extract the gravity anomaly indicating the ore-controlling geological factors and granites in a tin–copper polymetallic ore field; Asl and Manaman [31] proposed to utilize the modified EMD method for locating magnetic bodies by extracting the IMFs of the magnetic data; and Animesh and Shankho [32] applied BEMD in delineating gravity signatures related to complex near-surface features from noisy gravity data.

However, EMD suffers from several limitations, including sensitivities to meaningless fluctuations and irregularly spaced data, which distort the subsequent decomposition results [33–37]. In this regard, statistical EMD (SEMD) has been developed as an improvement over the traditional EMD method [33,34]. SEMD addresses these limitations by using a smoothing technique instead of an interpolation when constructing upper and lower envelopes to improve the reliability of the IMFs. This allows for a more accurate and robust decomposition of irregularly spaced signals with outliers and very high-frequency components, making it a useful tool for analyzing and processing real-world data [33]. The SEMD method is increasingly applied in many fields and has been shown to outperform EMD in various applications, including financial time series analysis [38,39], biomedical signal processing [40], and isolating geochemical logging data [41]. Nevertheless, the performance of SEMD depends on the choice of the smoothing technique used for constructing the upper and lower envelopes, which accordingly define the upper and lower bounds of the IMFs and thus can affect the accuracy of the decomposition [33,34]. If the smoothing method is not appropriate, the envelopes may be too smooth or too rough, resulting in the generation of inaccurate IMFs or the loss of important features in the signal. The envelopes are typically estimated using a cubic spline or local polygon smoothing techniques [33]. These methods can yield different results, particularly in regions where the signal has sharp transitions or discontinuities [42–44]. In this regard, the selection of an appropriate smoothing method in SEMD should be carefully considered based on the characteristics of the signal and the intended use of the IMFs.

Therefore, to validate its applicability, the novel SEMD method was applied to separate multi-scale gravity and magnetic anomalies from the background. The sensitivities of smoothing methods in SEMD to the combination and arrangement patterns of source fields including size, depth, and distance were investigated and compared using the numerical forward modeling method. In the case study, an SEMD method adopting a local polynomial smoothing approach was applied to process the aerial gravity and magnetic data in the eastern Tianshan orogenic belt for the decomposition of regional and local anomalies, which were used to gain insight into regional tectonics and mineral prospectivity.

2. Methods

2.1. SEMD Method

The EMD method, which was originally proposed by Huang in 1998 [14], is a data-driven and adaptive time-frequency analysis method for analyzing nonlinear and nonstationary signals. It decomposes a signal into a finite number of IMFs that correspond to different scales or frequency components of the signal. Each IMF is defined as an oscillatory wave that satisfies two conditions: having the same number of extrema (maxima and minima) and the same number of zero crossings, or differing by one, and its envelopes

connected by the local maxima and minima of the signal being symmetric with respect to zero. The SEMD is an extension of EMD designed to handle complex signals with noninformative fluctuations, such as noisy fluctuations and outliers, and irregularly spaced data [33]. The difference between SEMD and EMD is only in the way of extracting the first IMF, where a smoothing technique has been applied instead of an interpolation method.

2.1.1. Sifting Process

The sifting process (Figure 1) of SEMD for obtaining IMFs can be summarized as follows [33]:

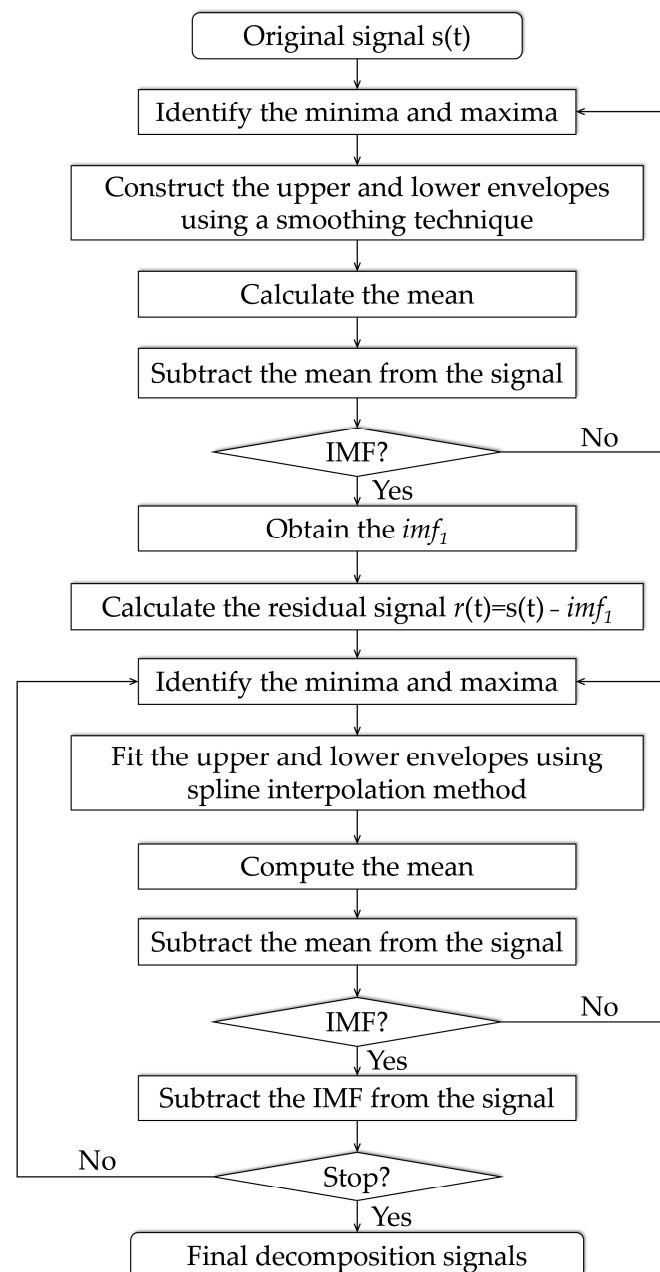


Figure 1. Sifting process of the SEMD method.

- (1) Identify the local maximum and minimum values Ω of the signal $h_{1,\alpha}^0(t)$, where $h_{1,\alpha}^0(t)$ represents the original signal $s(t)$ and t is the time.

- (2) Construct the upper envelope $\Omega_{\alpha}^{+}(t)$ and lower envelope $\Omega_{\alpha}^{-}(t)$ of the signal by using a smoothing technique with a smoothing parameter α to the maximum and minimum values Ω .

- (3) Calculate the mean of the upper and lower envelopes:

$$m_{\alpha}(t) = \frac{1}{2} [\Omega_{\alpha}^{+}(t) + \Omega_{\alpha}^{-}(t)] \quad (1)$$

- (4) Subtract the mean from the original signal to obtain an updated signal:

$$h_{1,\alpha}^1(t) = h_{1,\alpha}^0(t) - m_{\alpha}(t) \quad (2)$$

- (5) Perform steps 1–4 on the updated signal until the resulting signal $h_{1,\alpha}^j(t)$ at the j th iteration satisfies the above-mentioned IMF conditions and thereafter the first IMF, namely $imf_{1,\alpha}(t)$, is obtained.

- (6) Subtract $imf_{1,\alpha}(t)$ from the original signal to obtain the residual signal:

$$r_{\alpha}(t) = s(t) - imf_{1,\alpha}(t) \quad (3)$$

- (7) Use $r_{\alpha}(t)$ as the updated original signal and find all its local maxima and minima.

- (8) Fit the local maxima and minima to create the upper envelope $u(t)$ and lower envelope $l(t)$ of the signal accordingly using the cubic spline interpolation method.

- (9) Compute the mean of the upper and lower envelopes:

$$m_2(t) = \frac{1}{2} [u(t) + l(t)] \quad (4)$$

- (10) Subtract the mean from the original signal to obtain an updated signal:

$$h_2(t) = r_{\alpha}(t) - m_2(t) \quad (5)$$

- (11) Iterate steps 7–10 on the updated signal until the resulting signal satisfies the above-mentioned IMF conditions, and thereafter the second IMF, denoted as $imf_2(t)$, is derived.

- (12) Separate the second IMF from the original signal to obtain a residual signal:

$$r_2(t) = r_{\alpha}(t) - imf_2(t) \quad (6)$$

- (13) Update the original signal to $r_2(t)$ in step 7 and repeat steps 7–12 on the residual signal to obtain another IMF.

- (14) Continue the sifting process until the updated or residual signal is less than the predetermined value of substantial consequence, or no more IMFs can be extracted from the residual signal.

By performing the sifting process on the signal, SEMD separates the signal into different IMF components that correspond to different time scales or frequencies of the signal. These IMFs can then be further analyzed or processed separately to extract useful information from the signal.

2.1.2. Smoothing Technique

In this study, the two most commonly used smoothing techniques, which are cubic spline smoothing and local polynomial smoothing, have been applied in the SEMD method. Their basic principles may be summarized as follows:

- (1) Cubic spline smoothing is a useful technique for smoothing data by fitting a piecewise cubic function to the data points [45,46]. Each cubic spline function can be defined as:

$$\tilde{s}_i(t) = a_i + b_i(t - t_i) + c_i(t - t_i)^2 + d_i(t - t_i)^3 \quad (7)$$

where a , b , c , and d are undetermined coefficients. This method involves constructing a set of cubic polynomials that approximate the data, ensuring that the resulting curve is smooth and continuous. Thus, it aims to minimize squared error and the curvature of cubic splines. This is expressed as:

$$\min \sum_{i=1}^n [s_i - \tilde{s}_i(t_i)]^2 + \lambda \int [\tilde{s}''(t)]^2 dt \quad (8)$$

where λ is the smoothing parameter, the value of which is non-negative and not greater than one. If $\lambda = 0$, the curvature constraints are lifted, and the smoothing cubic spline then passes through all data points, resulting in an interpolation cubic spline.

- (2) Local polynomial smoothing smooths a signal by fitting a polynomial function to a localized subset of data points [45–48]. The local polynomial can be expressed as:

$$\hat{p}_i(t) = \beta_0 + \beta_1(t_i)t + \beta_2(t_i)t^2 + \cdots + \beta_p(t_i)t^m = \sum_{n=0}^m \beta_n(t_i)t^n \quad (9)$$

where β_0 , β_1 , \cdots , and β_p are the coefficients to be estimated. This smoothing method tries to use a weighted least squares approach to find the polynomial coefficients that minimize the sum of squared errors between the observed values and the predicted values. The weights are determined by a weighting function that assigns larger weights to nearby observations and smaller weights to distant ones. Thus, local polynomial fitting can be solved as a minimize problem given by:

$$\min \sum_{t_i \in T_i} \kappa \left(\frac{t_i - t_j}{h} \right) \left[s_i - \sum_{n=0}^m \beta_n(t_i)t_i^n \right]^2 \quad (10)$$

where κ denotes a non-negative weight function and h is the bandwidth controlling the size of the local neighborhood. By fitting the localized data, local polynomial smoothing can provide a smoothed curve that adapts to the local behavior of the data, allowing for more flexibility in capturing variations and features in the dataset.

2.2. Forward Model

To validate the applicability of SEMD in identifying gravity and magnetic anomalies and clarifying their geological significance, the forward modeling method has been used to generate synthetic data for the decomposition. The coordinate system was designed as shown in Figure 2, where the horizontal axis x represents distance, and the vertical axis h represents depth. There are three square field sources and their central coordinate values are (x_a, h_a) , (x_b, h_b) , and (x_c, h_c) , respectively. The sizes of these three field sources are a , b , and c , respectively. The density and magnetic susceptibility of the three blocks are set to 2.77 g/cm^3 and 0.01 SI , respectively. These properties for the background are defined to be 2.67 g/cm^3 and 0.00 SI , respectively. In this regard, the three field sources are assumed to have the same constant positive residual density and magnetic susceptibility, which are equal to 0.1 g/cm^3 and 0.01 SI , respectively.

In this study, a total of 36 forward models are constructed by using the control variable method, and the effects of field source size (i.e., a , b , and c), depth (i.e., h_a , h_b , and h_c), and distance (i.e., $x_b - x_a$ and $x_c - x_b$) on decomposition results are studied. These models are shown in Table 1. The 9 models that were labeled from M01 to M09 were designed to study the influence of field source size on SEMD. These models were assigned three sets of field sources with the same depth, and each set of models was arranged in three different sizes. The 9 models numbered from M10 to M18 were used to investigate the dependence of SEMD on field source depth. These models have three sets of field sources of the same size, with three depth arrangements for each set of the models. The 18 models numbered M19 to M36 are derived from three sets of models with the same field source size and different depths. Examples of these models highlight the impact of the relative distances between the models on SEMD. The SEMD method was used to decompose the synthetic data simulated by each of the designed models. As mentioned above, two smoothing

techniques, cubic spline and local polynomial, were used in the sifting process of the SEMD. The advantages and disadvantages of these two smoothing methods were studied by comparing the decomposition results.

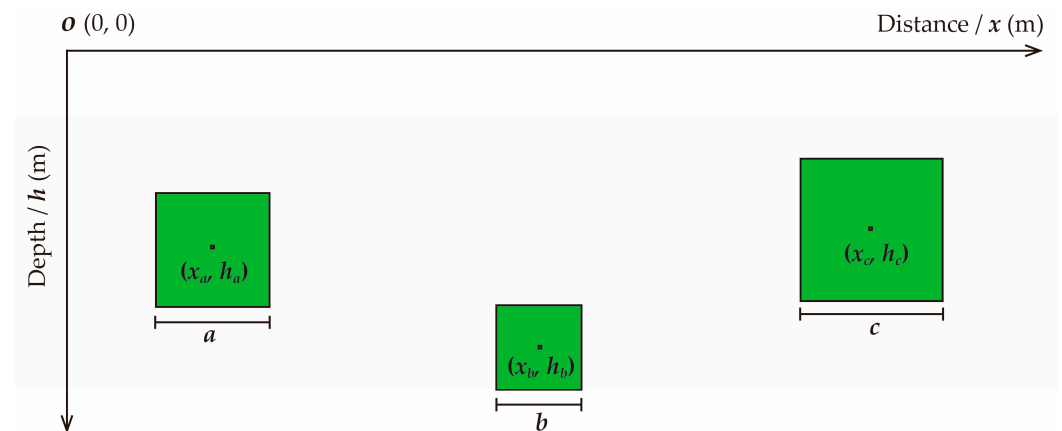


Figure 2. Field sources assigned in the forward model.

Table 1. Size, depth, and distance of field sources in the designed forward models.

Model	Size (m)			Depth (m)			Distance (m)
	a	b	c	h_a	h_b	h_c	
M01	50	100	150	100	100	100	200
M02	50	150	100	100	100	100	200
M03	100	50	150	100	100	100	200
M04	50	100	150	150	150	150	200
M05	50	150	100	150	150	150	200
M06	100	50	150	150	150	150	200
M07	50	100	150	200	200	200	200
M08	50	150	100	200	200	200	200
M09	100	50	150	200	200	200	200
M10	50	50	50	100	150	200	200
M11	50	50	50	100	200	150	200
M12	50	50	50	150	100	200	200
M13	100	100	100	100	150	200	200
M14	100	100	100	100	200	150	200
M15	100	100	100	150	100	200	200
M16	150	150	150	100	150	200	200
M17	150	150	150	100	200	150	200
M18	150	150	150	150	100	200	200
M19	50	50	50	100	200	150	50
M20	50	50	50	100	200	150	100
M21	50	50	50	100	200	150	150
M22	50	50	50	100	200	150	250
M23	50	50	50	100	200	150	300
M24	50	50	50	100	200	150	350
M25	100	100	100	150	100	200	100
M26	100	100	100	150	100	200	150
M27	100	100	100	150	100	200	250
M28	100	100	100	150	100	200	300
M29	100	100	100	150	100	200	350
M30	100	100	100	150	100	200	400
M31	150	150	150	100	150	200	150
M32	150	150	150	100	150	200	250
M33	150	150	150	100	150	200	300
M34	150	150	150	100	150	200	350
M35	150	150	150	100	150	200	400
M36	150	150	150	100	150	200	450

3. Results and Discussion

3.1. Forward Modeling

3.1.1. The Size of Field Sources

Figure 3 shows the IMFs obtained by decomposing the simulated gravity and magnetic data of the M01 to M09 forward models using the SEMD methods adopting cubic spline and local polynomial smoothing techniques, respectively. The SEMD methods can decompose more magnetic models than gravity models, regardless of the smoothing approach. The reason may be that under the same field source conditions, including size, depth, and distance, magnetic signals have larger fluctuation than gravity signals. In these decomposable forward models, no matter the gravity or magnetic data, they are more likely to be decomposed by the local-polynomial-based SEMD method rather than the cubic-spline-based approach. SEMD based on local polynomial smoothing can identify at least one IMF in most of the tested models. For example, the gravity (Figure 4) and magnetic (Figure 5) data of the M03 forward model can utilize the SEMD method adopting the local polynomial smoothing technique to decompose the long-wave and short-wave anomalies that represent and interpret the source features. However, this cannot be achieved using the SEMD method with the cubic spline smoothing approach. Figures 4a and 5a show that the IMF1 signal could identify two peaks that indicate the positive gravity and magnetic anomalies caused by the two larger blocks (i.e., the field sources a and c, respectively). Nevertheless, the responses of both gravity and magnetic fields for the smallest source (i.e., the b block) have been ignored, because there are no more IMFs decomposed to characterize the anomalies. The residual signals (Figures 4a and 5a) mainly characterize the total density and magnetic susceptibility contrasts between the three field sources and the background, respectively. Figures 4b and 5b indicate that the IMF1 signal could hint at the gravity and magnetic anomalies produced by the two larger field sources, respectively. The gravity and magnetic anomalies caused by the smallest field source (i.e., the b blocks) could not be distinguished. Thus, these results indicate that the SEMD method using the local polynomial smoothing technique is more applicable for identifying multi-scale anomalies, which are hidden in the complex gravity and magnetic survey signals.

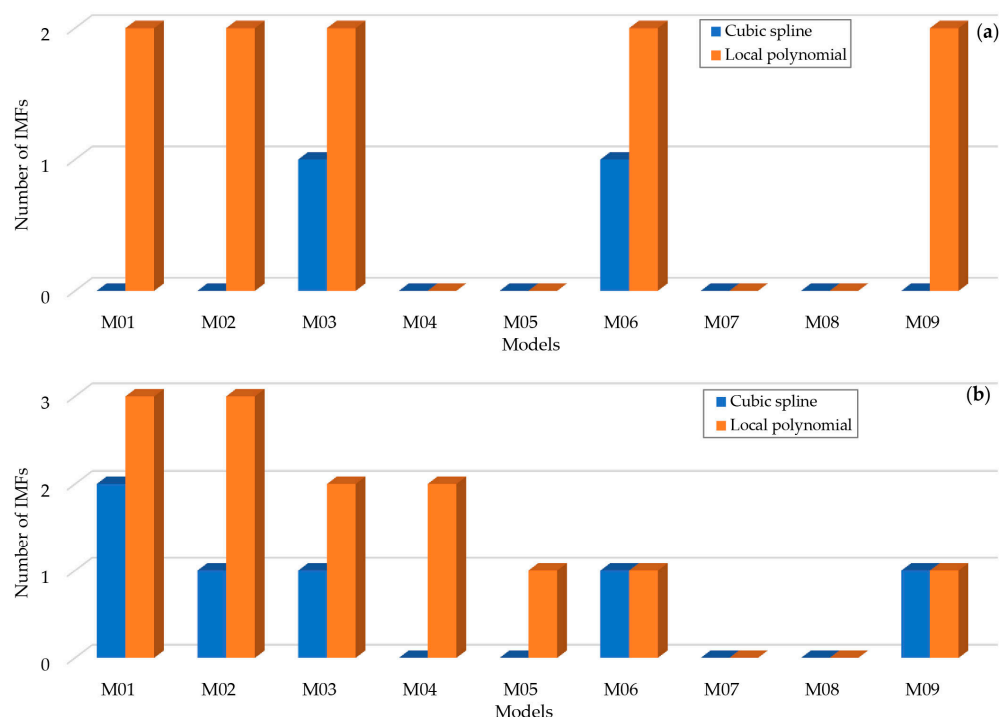


Figure 3. Bar diagrams showing the IMFs derived by decomposing the simulated gravity (a) and magnetic (b) data of the M01 to M09 forward models using SEMD.

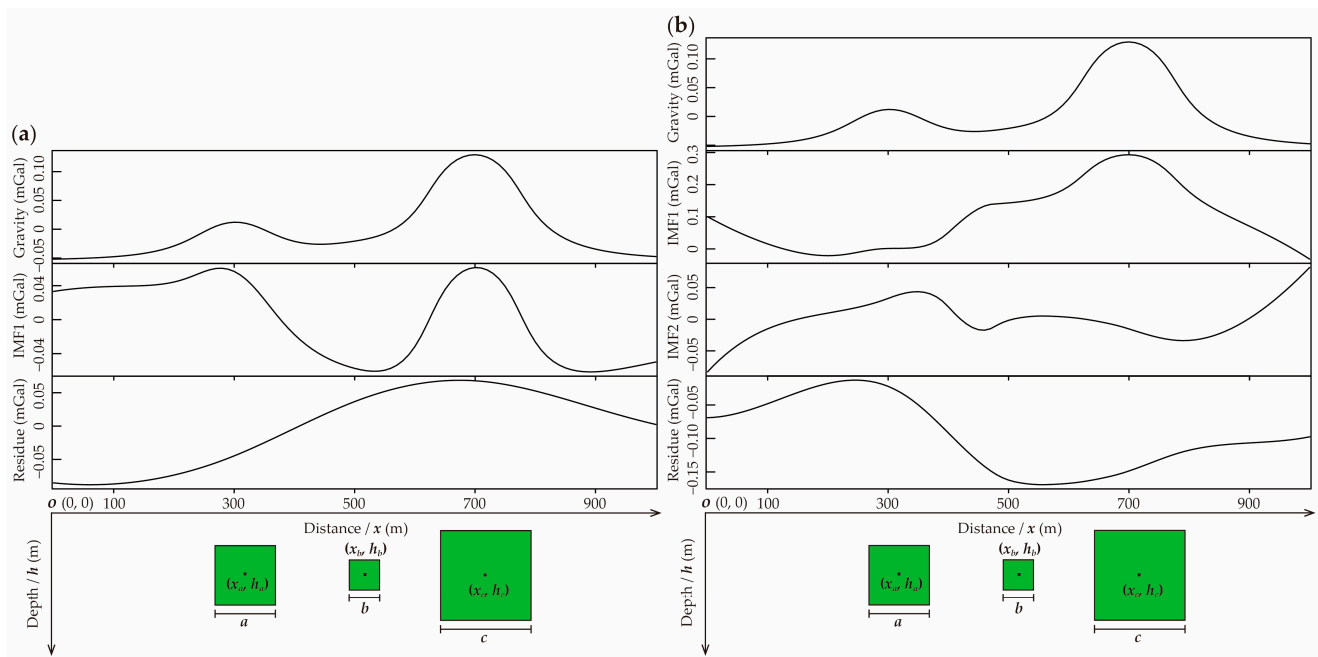


Figure 4. Decomposition results of the simulated gravity data of the M03 forward model using SEMD adopting the cubic spline (a) and local polynomial (b) smoothing techniques.

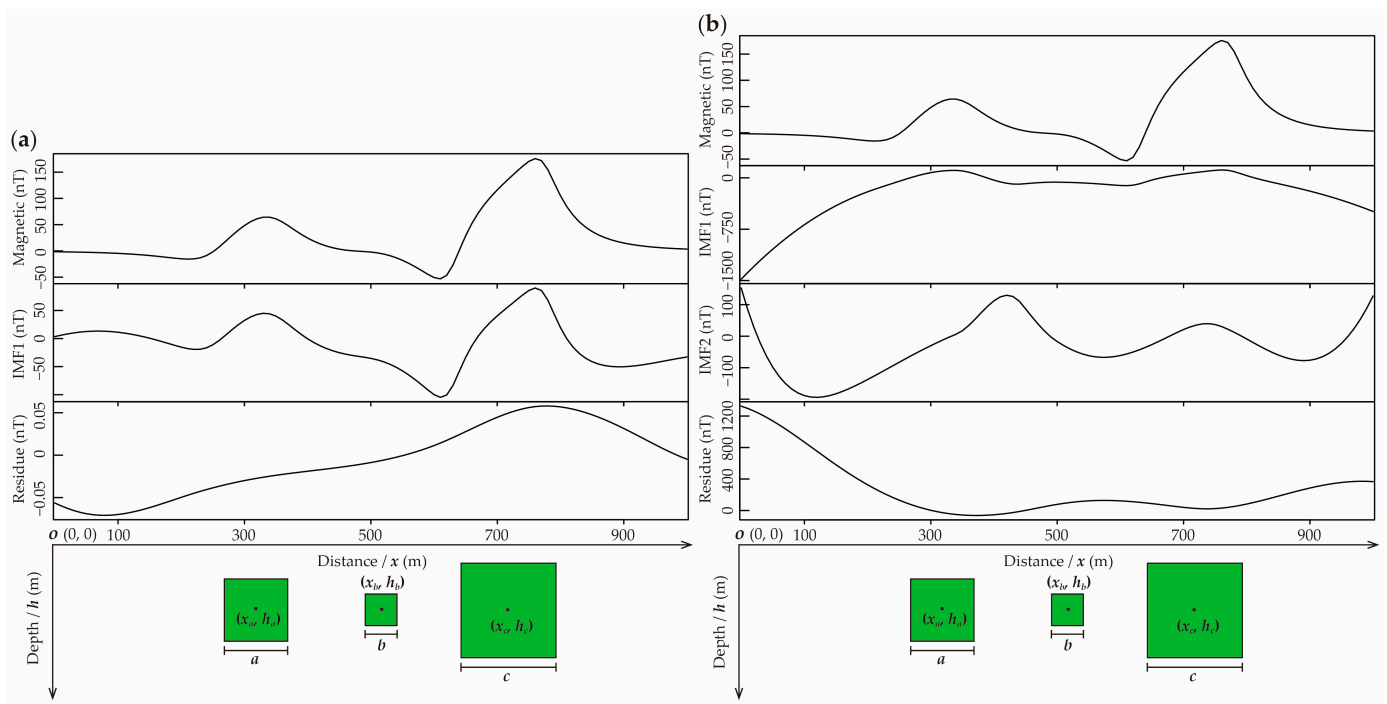


Figure 5. Decomposition results of the simulated magnetic data of the M03 forward model using SEMD adopting the cubic spline (a) and local polynomial (b) smoothing techniques.

3.1.2. The Depth of Field Sources

Figure 6 shows the IMFs decomposed by the SEMD methods, which were applied to the simulated gravity and magnetic data of the M10 to M18 forward models using the cubic spline and local polynomial smoothing techniques, respectively. It also shows that most of the models, no matter gravity and magnetic data, can be decomposed by the SEMD method using local polynomial smoothing rather than that using cubic spline smoothing. In the decomposable models, more were extracted by the SEMD method

adopting the polynomial smoothing technique with two IMFs. Considering the residual components, these decomposition results are consistent with the number of field sources set in the forward model. This indicates that the SEMD method may have correctly identified individual anomalies caused by these field sources. For example, the IMFs identified by the SEMD method using the local polynomial smoothing technique from the gravity (Figure 7b) and magnetic (Figure 8b) data of the M14 forward model indicate anomalous features of the field sources, while the SEMD method adopting the cubic spline smoothing approach cannot separate enough IMFs from the mixed signal (Figures 7a and 8a). Figures 7a and 8a show that the anomalies of both gravity and magnetic fields for the sources at shallow and moderate depth (i.e., blocks a and c) can be identified, whereas the anomalies from the deepest source (i.e., the b block) are also ignored, as shown in the model M03 mentioned above. The residual signals (Figures 7a and 8a) characterize the long-wave anomalies caused by the total contrast of density and magnetic susceptibility between the field sources and background. Figures 7b and 8b indicate that the gravity and magnetic anomalies from the shallow source (i.e., block a) could be identified from the IMF1 signals, and the anomalies from the moderate depth and deep sources can be trailed by the IMF2 signals. Therefore, it can be considered that the SEMD method adopting local polynomial smoothing is more useful than that adopting cubic spline smoothing for identifying multi-scale gravity and magnetic anomalies.

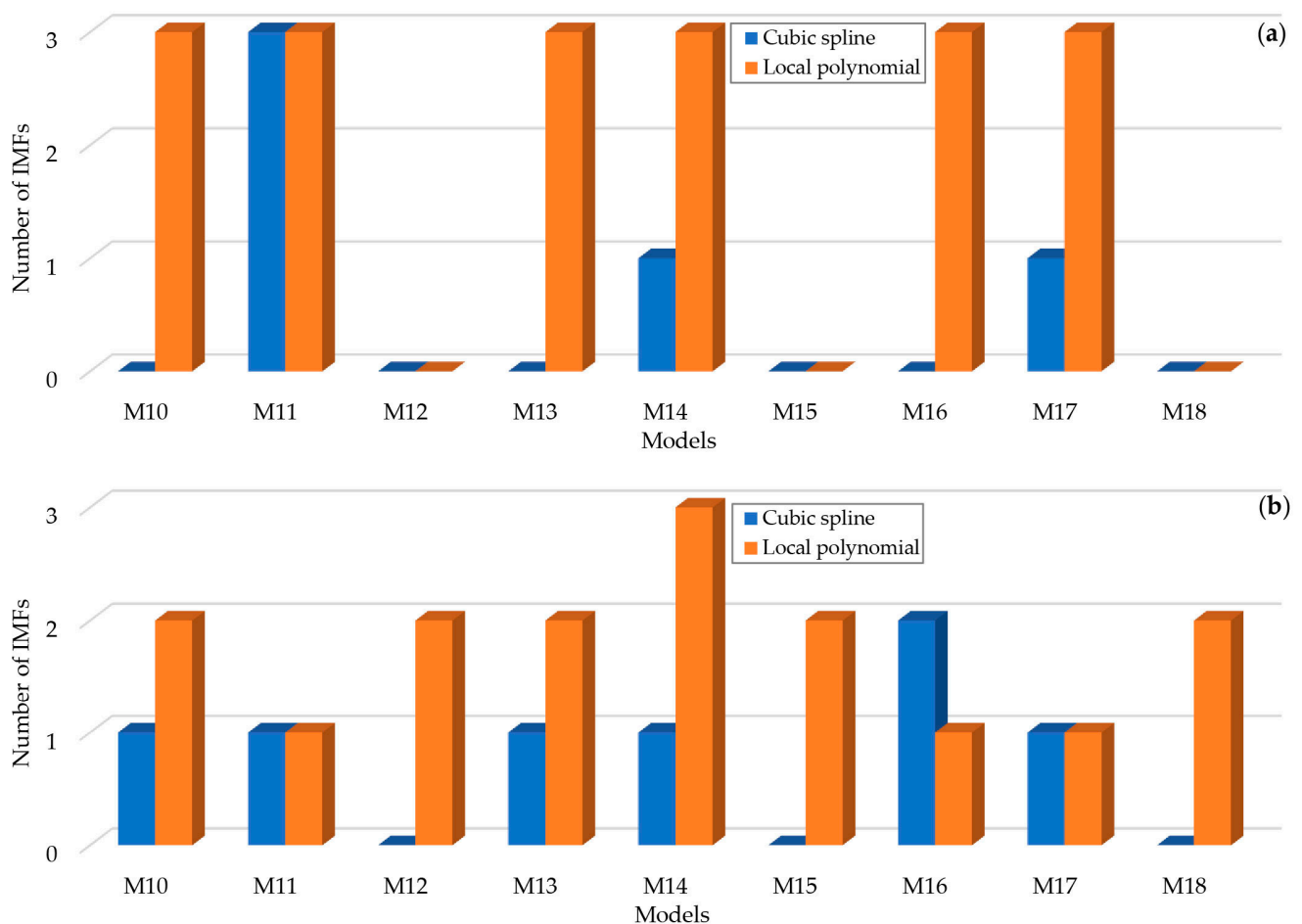


Figure 6. Bar diagrams showing the IMFs derived by decomposing the simulated gravity (a) and magnetic (b) data of the M10 to M18 forward models using SEMD.

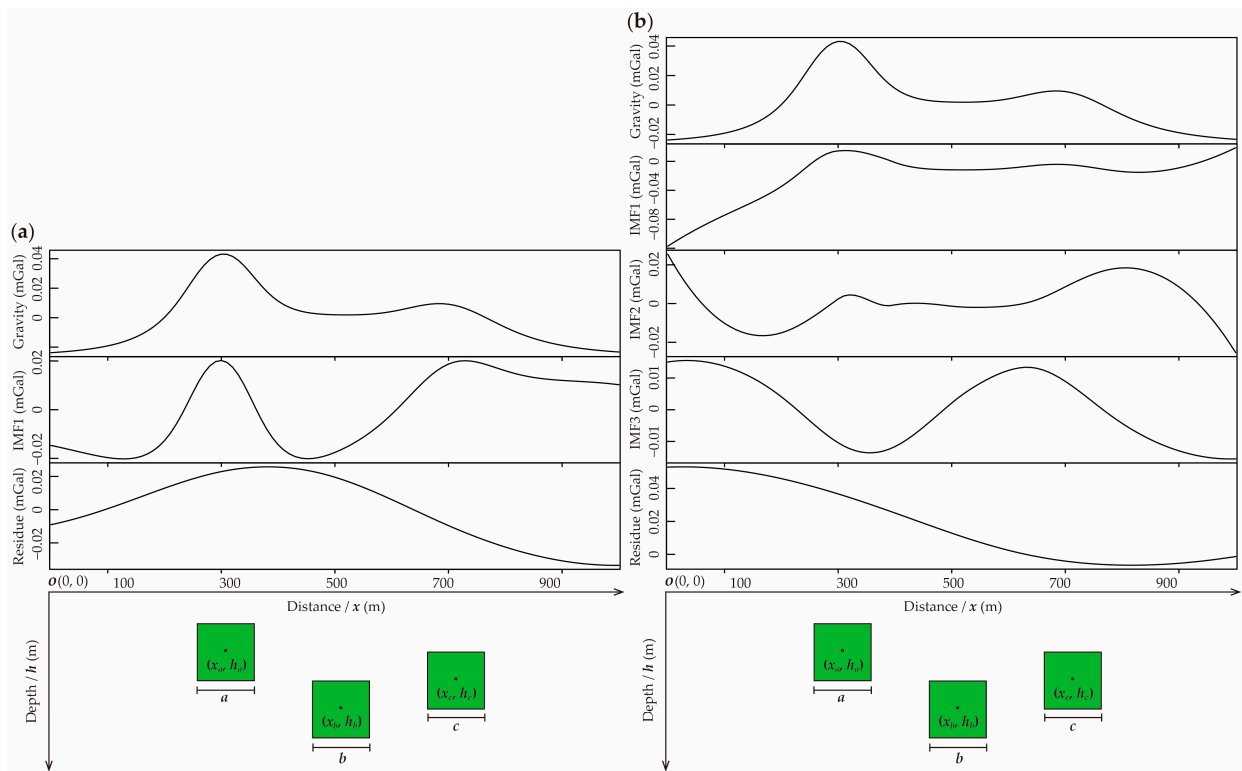


Figure 7. Decomposition results of the simulated gravity data of the M14 forward model using SEMD adopting the cubic spline (a) and local polynomial (b) smoothing techniques.

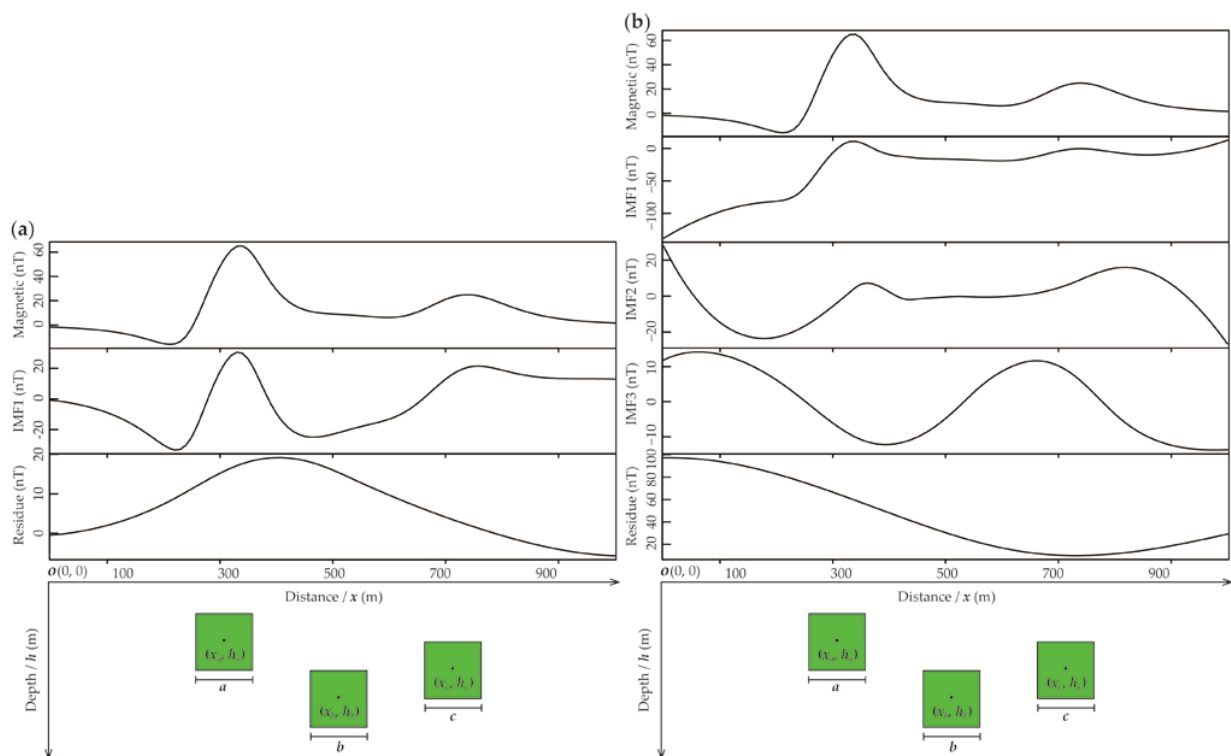


Figure 8. Decomposition results of the simulated magnetic data of the M14 forward model using SEMD adopting the cubic spline (a) and local polynomial (b) smoothing techniques.

3.1.3. The Distance between Field Sources

To investigate in more detail the dependence of SEMD on field source distance, the decomposition results of the M18 to M36 models were compared and shown in Figure 9. These 18 models have been classified into three groups, which accordingly represent three types of models with characterized sizes and depths. Compared to the models with small field source distances, regardless of their size and depth, the models with large field source distances are not only more likely to be successfully decomposed by the SEMD methods but also the number of the decomposed IMFs is closer to that of field sources set in the forward models. Therefore, forward modeling shows that increasing the distance between field sources seems to be beneficial for the decomposition of the synthetic signal they cause using SEMD. This can be explained as that, the larger the distance between individual field sources, the smaller the superposition effects between the signals produced by these fields, resulting in more significant differences in signal extrema and frequencies at different field sources, and vice versa. This is like many geophysical signal processing methods. In addition, the decomposable models indicate that the SEMD method using local polynomial smoothing is more applicable than that using cubic spline smoothing. This is because the SEMD method adopting local polynomial smoothing can generally decompose IMFs that are equivalent to the number of field sources. On the contrary, cubic spline smoothing possibly introduces spurious oscillations in the envelopes, which can affect the accuracy of the IMFs. The reasons include the fact that many models cannot be decomposed by the SEMD method using cubic spline smoothing, and there is a model (i.e., M22) that has been decomposed into too many IMFs (Figure 9b). In addition, Figure 10a shows that the pattern of the IMF1 signal is almost the same as the original gravity data, indicating that SEMD adopting the cubic spline smoothing technique may not be able to effectively decompose the mixed gravity signal. Figures 10b and 11b illustrated that the peaks for the IMFs of both gravity and magnetic data derived by the SEMD using the local polynomial smoothing technique could locate the field sources of the forward model. Furthermore, the interpretations of the interpretable IMFs and residual signals for the M22 model are essentially similar to those for the M14 model. This similarity arises due to the identical arrangement of field sources in both models, with the only difference being the varying size and spacing distance of the field sources. Nevertheless, it has been demonstrated by comparison of the decomposition results between these two models that the larger the distance between field sources, the more favorable it is for the mixed signal to be decomposed into simple form signals, as the increase in the distance between field sources leads to a decrease in the degree of mixture between their gravity and magnetic signals.

3.2. Case Study: Identifying the Multi-Scale Gravity and Magnetic Anomalies of the Eastern Tianshan Orogenic Belt

3.2.1. Geological Setting and Data

The eastern Tianshan is in the southern part of the world-famous orogenic belt, namely the Central Asia orogenic belt (CAOB), which is formed by the amalgamation of several blocks between the Siberia and Tarim–North China cratons [49–53]. This district has a long and complex history of tectonic activity, resulting in a wide range of rock types and structures (Figure 12a). The oldest rocks in the eastern Tianshan orogenic belt are exposed in the northwestern part of the belt and mainly consist of granitic gneisses and schists that were formed during the Precambrian. The Paleozoic sequence consists of a series of sedimentary rocks that were deposited during the Devonian, Carboniferous, and Permian periods. These rocks are exposed throughout the belt and include sandstones, shales, and limestones. The Mesozoic is characterized by a series of granitic intrusions that were emplaced during the Jurassic and Cretaceous periods. These intrusions have been demonstrated to serve as sources of mineralization, including copper, gold, and molybdenum [54–56]. The Cenozoic is represented in the eastern Tianshan orogenic belt by a series of sedimentary basins that were formed during the Tertiary period. These basins

are characterized by thick sequences of sedimentary rocks, including sandstones, shales, and conglomerates, that were deposited in fluvial, lacustrine, and deltaic environments.

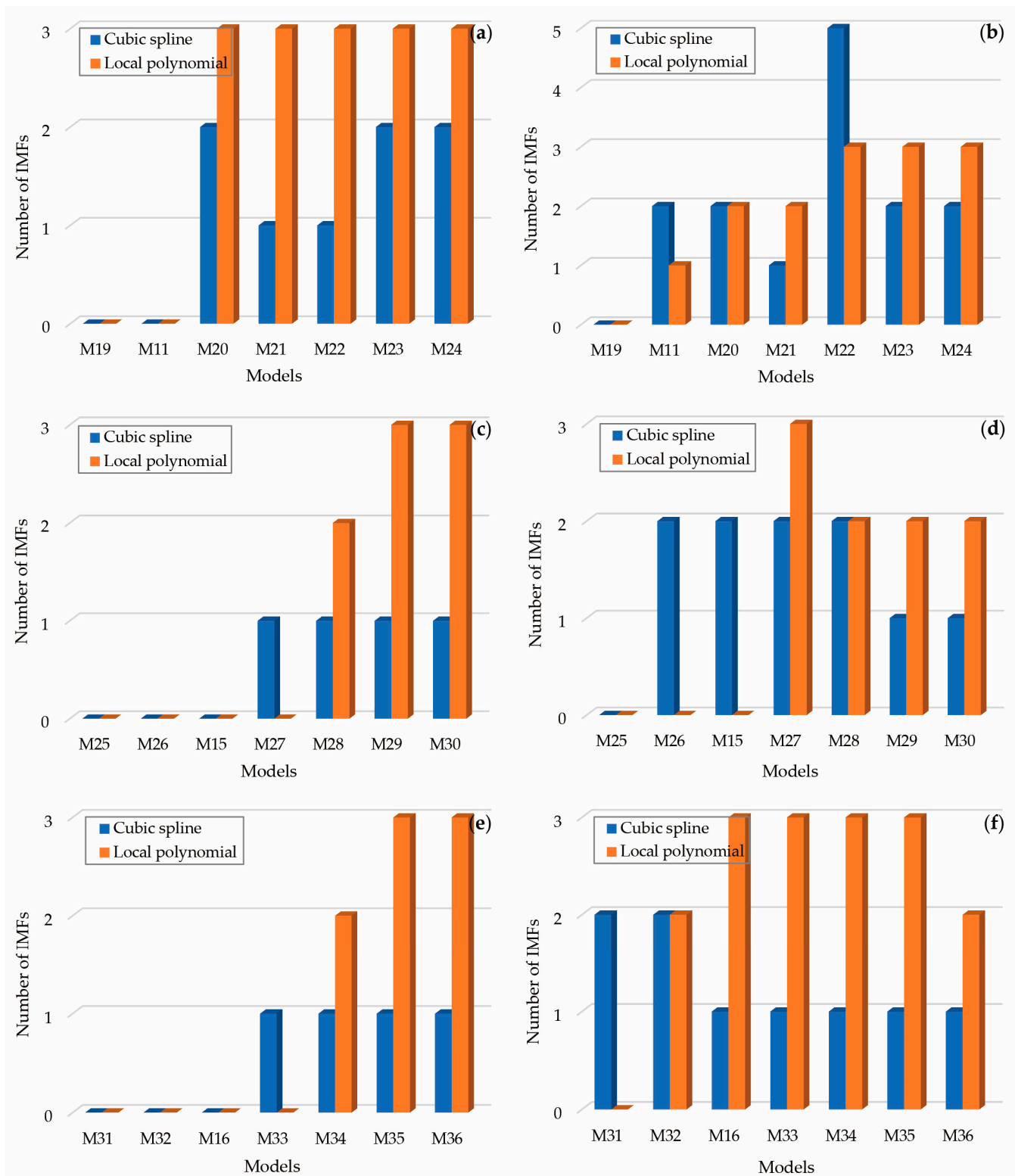


Figure 9. Bar diagrams showing the IMFs derived by decomposing the simulated gravity (a,c,e) and magnetic (b,d,f) data of the M19 to M36 forward models using SEMD.

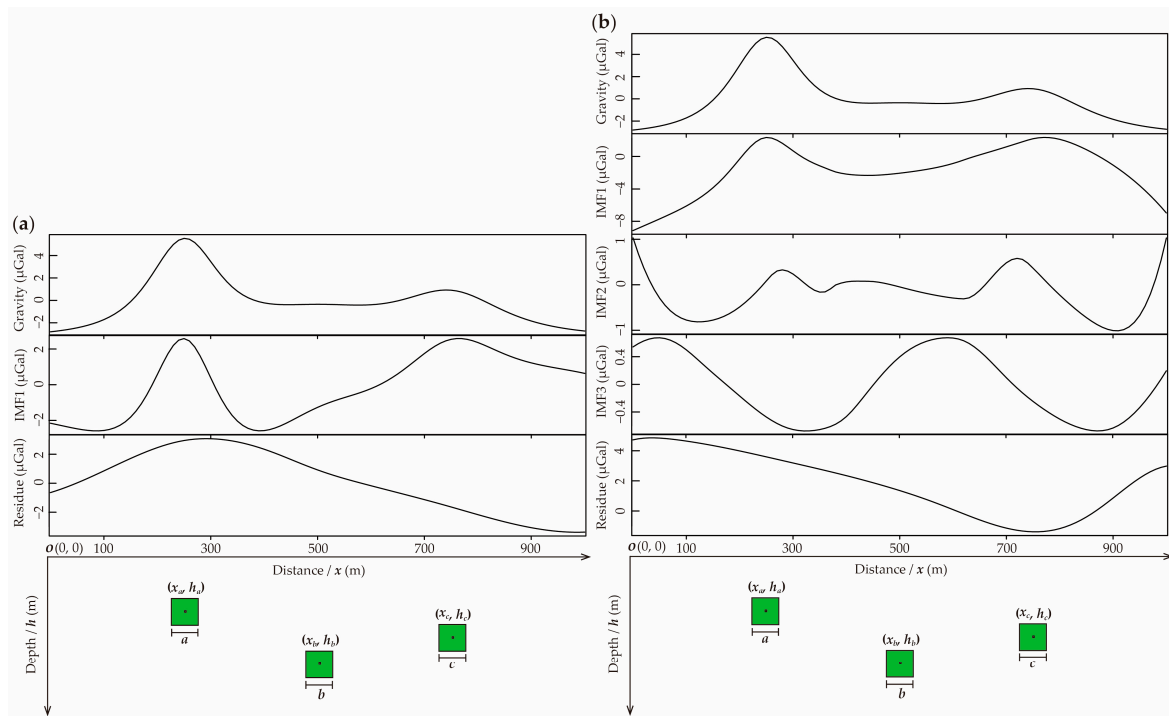


Figure 10. Decomposition results of the simulated gravity data of the M22 forward model using SEMD adopting the cubic spline (a) and local polynomial (b) smoothing techniques.

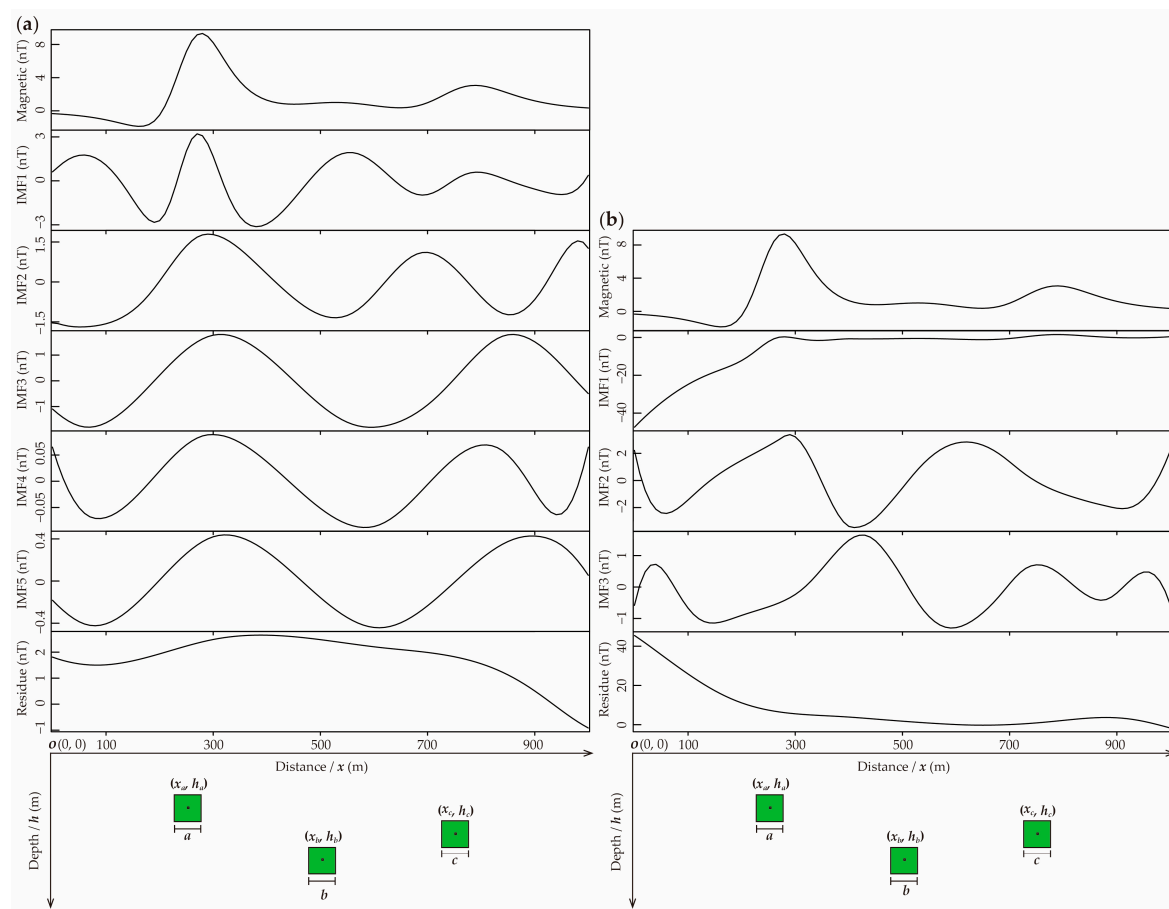


Figure 11. Decomposition results of the simulated magnetic data of the M22 forward model using SEMD adopting the cubic spline (a) and local polynomial (b) smoothing techniques.

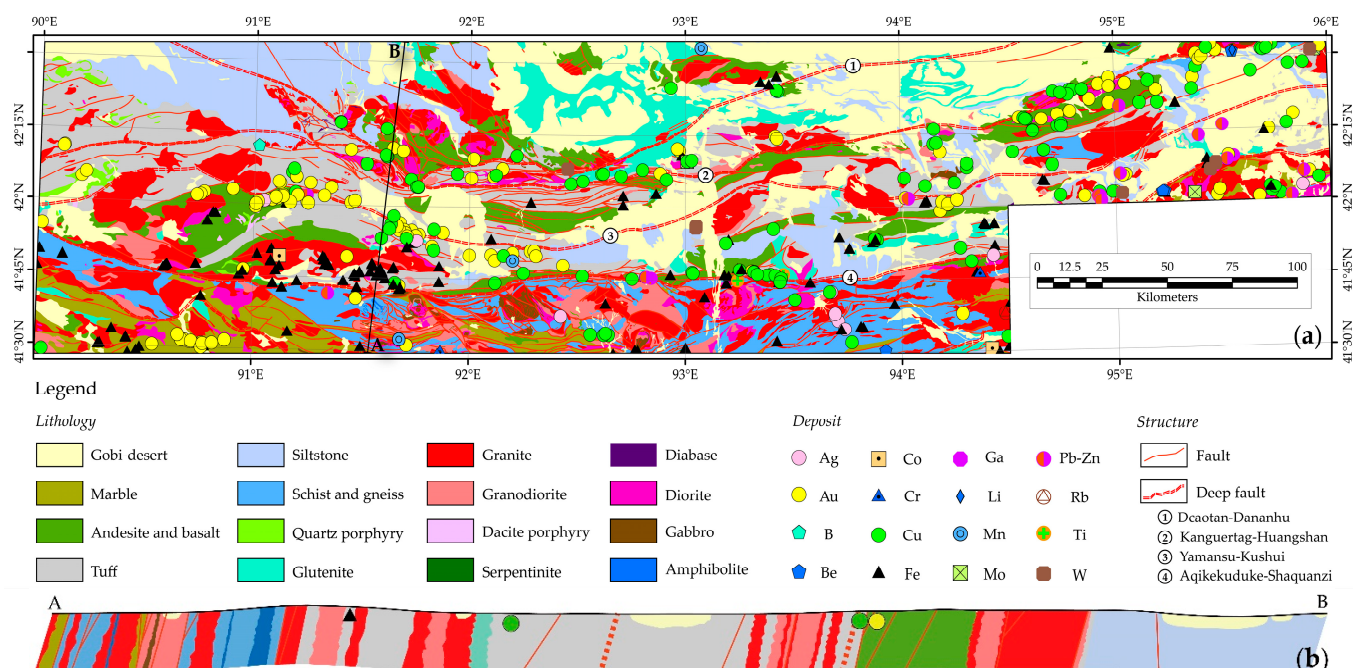


Figure 12. Simplified geological map (a) and the geological profile AB (b) where the decomposed aerial gravity and magnetic data are located.

There are four EW-trending deep faults identified in the eastern Tianshan region. They are, from north to south, the Dacotan-Dananhu, Kanguertag-Huangshan, Yamansu-Kushui, and Aqikekuduke-Shaquanzi faults. Separated by the Dacotan-Dananhu, Yamansu-Kushui, and Aqikekuduke-Shaquanzi faults, the eastern Tianshan orogenic belt can be divided into four main tectonic units. They are the Dananhu-Tousuquan arc belt, the Kanguertag-Huangshan forearc/intra-arc basin belt, the Aqishan-Yamansu forearc basin belt, and the Middle Tianshan arc belt, respectively (Figure 12a). The Dananhu-Tousuquan arc belt is located within the southern margin of the eastern Tianshan orogenic belt. It formed in the Late Paleozoic, specifically during the Carboniferous to Permian period [49]. The arc belt consists of a series of volcanic rocks including andesite, dacite, rhyolite, plutonic, and sedimentary rocks. Most of this arc belt has been covered by the Gobi Desert layer. The Kanguertag-Huangshan forearc/intra-arc basin belt is on the southern side of the Dananhu-Tousuquan arc belt. It is a complex basin system composed of a variety of rock types, including sedimentary and volcanic rocks. The basin system is believed to have formed in the Late Paleozoic because of the subduction of the Paleo-Asian Ocean (PAO) under the southern margin of the CAO. The Aqishan-Yamansu forearc basin belt is situated south of the Kanguertag-Huangshan forearc/intra-arc basin belt. It is a complex basin system composed of a variety of rock types, including sedimentary and volcanic rocks. It is also considered to have formed due to the subduction of the PAO under the southern margin of the CAO during the Late Paleozoic. The Middle Tianshan arc, which is complex and includes a variety of rock types, including sedimentary, volcanic, and metamorphic rocks, is in the southern margin of the eastern Tianshan orogenic belt. The basement rocks in the study area are highly weathered, and there is a widespread distribution of eolian sand and loess. Nearly half of the area is covered by the Gobi Desert, including sand, soil, and gravel. This landscape severely hinders geological mapping in the eastern Tianshan area, and subsequently leads to significant challenges for structural analysis and mineral exploration [57]. Nevertheless, the eastern Tianshan region is well known for its diverse and extensive mineral resources, including a variety of different types of ore deposits [55,56,58,59]. The dominant metal minerals mainly include porphyry and magmatic sulfide-rich copper polymetallic deposits, epithermal and sedimentary rock-hosted gold deposits, and volcanic iron deposits [56].

To interpret the regional structure of the eastern Tianshan district, aerial gravity and magnetic data from an NS-trending profile AB (Figure 12a), which is generally perpendicular to the tectonic belts there, were decomposed by SEMD in this study. This geological profile is shown in Figure 12b. The gravity data were derived from Bouguer correction that has considered height, mass, and terrain effects in the measurement of natural gravity [1,3]. The aeromagnetic data have been processed utilizing the reduced-to-pole transformation method [2], which aligns magnetic anomalies with causative geological targets. The measurement points of these gravity and magnetic data are approximately 2 km apart.

3.2.2. Densities and Magnetic Properties of Lithologies

The densities and magnetic properties of rocks within a district are significant for interpreting gravity and magnetic data there [2]. Thus, the density data and magnetic properties data including both susceptibilities and remnant magnetizations of the major rock units in the eastern Tianshan region were collected from previous studies [50,60,61], and the results are shown in Table 2. The unconsolidated sediments of the Gobi Desert have the lowest densities, magnetic susceptibility, and remanent magnetization. Therefore, they are commonly believed to produce low gravity–magnetic anomalies. The density of sedimentary rocks, including siltstone and glutenite, is usually low to moderate, and their magnetic susceptibility and remanent magnetization are almost zero. Thus, the sedimentary rocks generally produce gravity anomalies ranging from low to medium, as well as low magnetic anomalies in the study area. The density and magnetic properties of intrusive rocks and volcanic rocks vary significantly with changes in their mineral composition. In general, mafic–ultramafic rocks that consist of many magnesium- and iron-bearing minerals and have few feldspathic minerals tend to have high density and magnetism, while intermediate–acidic rocks that are primarily composed of feldspathic minerals and contain almost no magnesium and iron-bearing minerals tend to have low density and magnetism. In this regard, mafic–ultramafic rocks have higher densities and magnetic properties compared to intermediate–acidic rocks. Metamorphic rocks such as gneiss, schist, marble, and amphibolite usually have relatively moderate to high densities, whereas they have very low magnetic susceptibility and remanent magnetization. Thus, the metamorphic rocks usually could produce moderate to high gravity anomalies and low magnetic anomalies in the eastern Tianshan district.

Table 2. The average density and magnetic properties of rocks from the eastern Tianshan district.

Lithology	Density (10^3 kg/m^3)	Magnetic Susceptibility ($10^{-6} \text{ 4}\pi\text{SI}$)	Remnant Polarization (10^{-3} A/m)
Gobi Desert	1.77	0.00	0.00
Marble	2.77	0.00	0.00
Andesite	2.75	N.A.	N.A.
Basalt	2.77	N.A.	N.A.
Tuff	2.68	950	550
Siltstone	2.66	0.00	0.00
Schist	2.68	76.0	60.0
Gneiss	2.67	N.A.	N.A.
Quartz porphyry	2.66	N.A.	N.A.
Glutenite	2.68	0.00	0.00
Granite	2.61	1079	N.A.
Granodiorite	2.68	50.0	0.00
Dacite porphyry	2.66	N.A.	N.A.
Serpentinite	2.93	3850	4600
Diabase	2.86	58,510	N.A.
Diorite	2.79	2872	N.A.
Gabbro	2.90	8330	1500
Amphibolite	2.79	N.A.	N.A.

N.A. means no data.

3.2.3. Multi-Scale Gravity and Magnetic Anomalies

The forward modeling results mentioned above indicate that the SEMD method using the local polynomial smoothing technique generally performs better in decomposing gravity and magnetic data than the method using cubic spline smoothing. Consequently, the SEMD method adopting the local polynomial smoothing technique was applied to decompose the gravity and magnetic data (Figure 12b) to identify multi-scale anomalies in the eastern Tianshan district.

Figure 13 shows the decomposition results of Bouguer gravity data. Three IMFs (i.e., IMF1, IMF2, and IMF3) from high to low frequencies and one residue signal were obtained. The IMF1 signal has a small amplitude, with its fluctuation range around -3 to 2 mGal, and a high frequency, which may reflect density differences in shallow geological bodies and/or noise components inherent in the data. The IMF2 signal has a moderate frequency and amplitude. The fluctuation range of the signal amplitude is approximately between -6 and 6 mGal, which has significant contrast and thus could indicate changes in lithology and/or the presence of metal mineral belts. For example, basins covered by the Gobi Desert generally exhibit significant gravity anomalies; areas dominated by granitic rocks show low gravity anomalies; areas with andesites and basalts exhibit high gravity anomalies; and the ore fields of iron, copper, and gold almost without exception display high gravity anomalies. The IMF3 signal most likely indicates anomalies caused by deep and large field sources, because it has a considerable amplitude ranging from approximately -15 to 15 mGal, and a very low frequency. This gravity anomaly signal has two peaks and two valleys. Compared with the geological profile, the IMF3 signal characterizes the structural framework of the eastern Tianshan district. The two long-wave anomalies with low amplitudes (i.e., signal valleys) are in the Kanggurtag forearc basin and the sedimentary basin on the north side of the Dananhu-Tousuquan arc belt, respectively, due to the relatively low density of sedimentary rocks. The two long-wave anomalies with high amplitudes (i.e., signal peaks) are located on the Middle Tianshan arc belt and the south side of the Dananhu-Tousuquan arc belt, respectively, because the basements of these two regions are metamorphic rocks and basic intrusions, respectively, both of which have relatively high densities in the eastern Tianshan area. The residual gravity anomaly signal has the largest amplitude, which varies from -164 to -140 mGal, and has a monotonic feature of being low in the south and high in the north. According to the forward modeling results, in which the residual signal anomalies characterize the changing trends of the density and magnetic susceptibility of the field sources, this gravity anomaly can explain the characteristic of the average density of the crust in the south being lower than that of the crust in the north of the study area. This is because there may be a large amount of high-density basalts intruded into the northern crust, although only a part of them is exposed.

Figure 14 shows the decomposition results of aeromagnetic data. Similar to gravity data, three IMFs (i.e., IMF1, IMF2, and IMF3) and one residual component signal have been identified. The frequency of these signals is decreasing in sequence. IMF1 and IMF2 have relatively large amplitudes, while IMF3 and the residual signals have relatively small amplitudes. Besides the noise component in the aeromagnetic survey data, IMF1 may indicate the magnetic contrast of shallow geological bodies, as the magnetic susceptibility and remnant polarization of these field sources with different lithologies in the study area can differ by one to two orders of magnitude. IMF2 characterizes regional magnetic anomalies of moderate depth, where high magnetic anomalies may be attributed to the presence of mafic intrusive rocks, including andesite and basalt, as well as marine volcanic rocks, and metal ore districts closely associated with these rock types. The mafic rocks are closely related to copper–nickel sulfide deposits. Marine volcanic rocks are the main ore-bearing strata for iron ore in the study area. Therefore, these factors collectively lead to the relatively high magnetic anomalies. The low magnetic anomalies indicated by the IMF2 signal correspond to the location of an intermediate–acid intrusion belt, normal sedimentary rocks, and the Gobi Desert-covered basin. The reason is that these rocks have

little or no magnetism. The long-wavelength anomalies characterized by the IMF3 signal indicate crustal-scale structural units. From south to north, the IMF3 signal alternates with two peaks and two valleys. The high anomaly in the south reflects the magnetic metamorphic basement of the Middle Tianshan arc, while the high anomaly in the north is likely caused by the deep, large-scale upwelling of mafic magma due to the junction of the Kanggurtag-Huangshan forearc/intra-arc basin and the Dananhu-Tousuquan arc. The low anomaly in the south primarily indicates the large-scale intermediate–acid magma activity of the Aqishan-Yamansu forearc basin belt. The low anomaly in the north mainly implies the sedimentary basin in the northern part of the Dananhu-Tousuquan arc. The residual component signal shows a monotonous magnetic anomaly trend of high in the north and low in the south. This shows information about the average magnetic susceptibility of the crust in the eastern Tianshan orogenic belt. The result indicates that the northern crust has stronger magnetism than the southern crust. This finding supports the interpretation result of the aforementioned residual gravity anomaly, indicating the possibility of large-scale mafic–ultramafic intrusions in the northern crust of the eastern Tianshan orogenic belt.

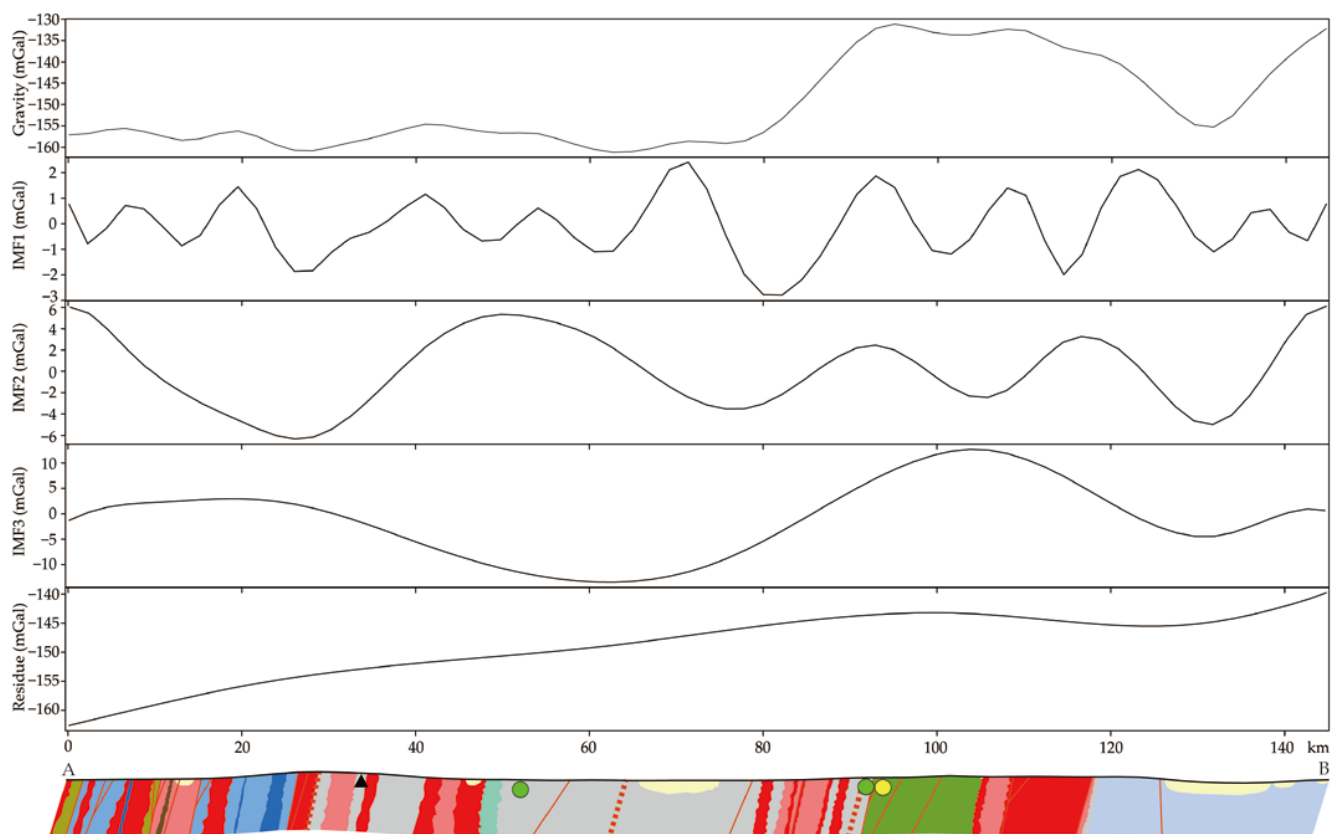


Figure 13. Decomposition results of Bouguer gravity data by SEMD. The bottom is the geological profile AB shown in Figure 12b.

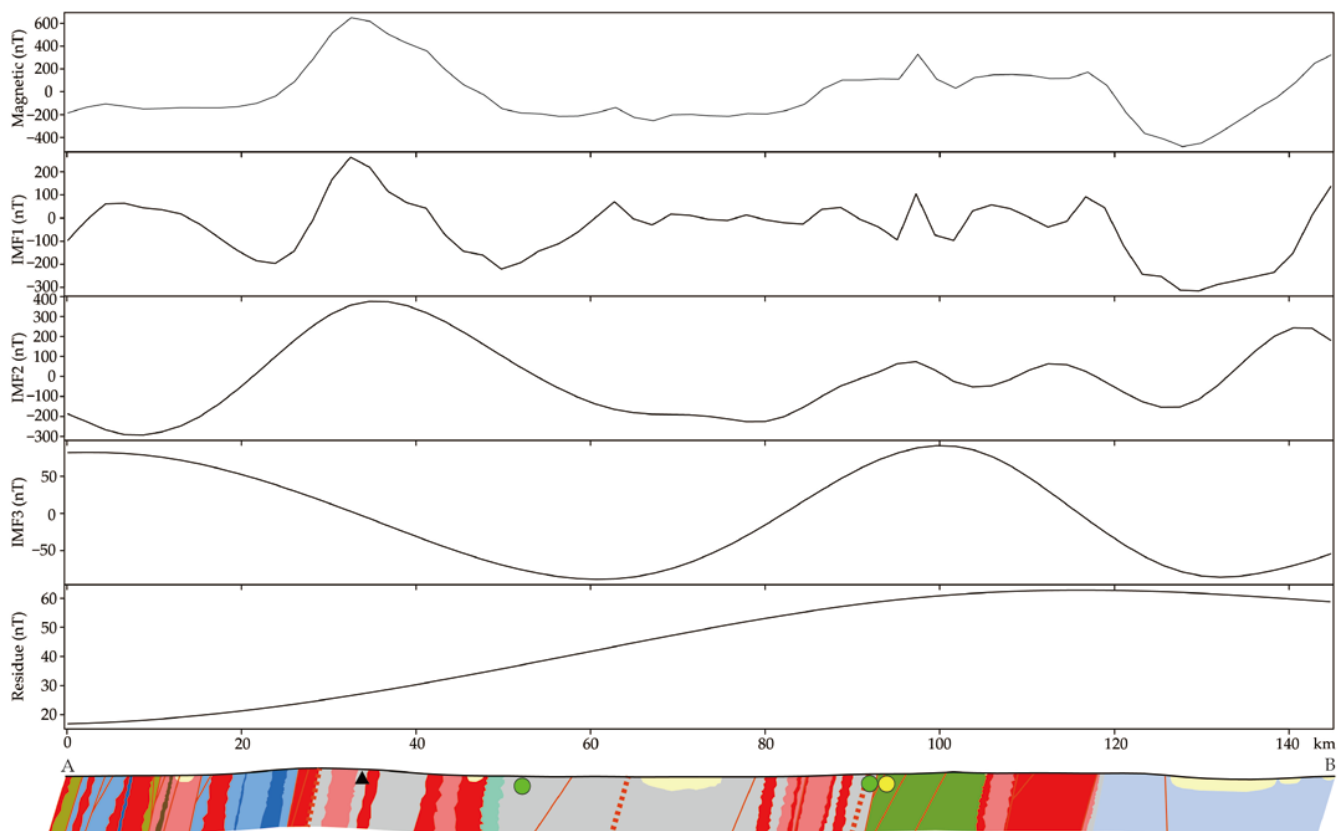


Figure 14. Decomposition results of aeromagnetic data by SEMD. The bottom is the geological profile AB shown in Figure 12b.

4. Conclusions

The current study used forward modeling data and actual aeromagnetic and gravity data from the eastern Tianshan region to verify the applicability of the SEMD method, which uses the cubic spline and local polynomial smoothing techniques, to identify multi-scale gravity anomalies. The main conclusions are as follows:

- (1) A comparison of forward modeling results shows that the SEMD method using the local polynomial smoothing technique performs better in decomposing gravity and magnetic data than the SEMD method using the cubic spline smoothing technique.
- (2) The decomposition results of aeromagnetic and gravity data in the eastern Tianshan district further demonstrate the effectiveness of the SEMD method using local polynomial smoothing in identifying multi-scale gravity anomalies. This method uses the smoothing technique to remove noise and extracts the high-frequency component (i.e., IMF1) that has almost no geological significance from the original signal. This is equivalent to denoising the original signal, eliminating the interference of meaningless fluctuations in the subsequent decomposition process, which could potentially contaminate all signals. Therefore, the remaining IMFs and residual component signals often have distinct geological significance and effectively reveal the regional scale and middle-to-deep level structural framework of the Gobi Desert-covered area in the eastern Tianshan region. Both the gravity and magnetic anomalies indicate that the junction zone of the Kanggurtag-Huangshan forearc/intra-arc basin and the Dananhu-Tousuquan arc may have the characteristics of a plate or block boundary. This provides more geophysical evidence to resolve the disputed issue of the division of the eastern Tianshan tectonic unit caused by the coverage of the Gobi Desert.

Author Contributions: Conceptualization, supervision, and writing—review and editing, F.X.; methodology and data processing, W.L.; visualization and writing—original draft preparation, H.Y.; discussion and editing, C.W. All authors have read and agreed to the published version of the manuscript.

Funding: This research was funded by the Ministry of Science and Technology of China (no. 2022YFF0801201) and the National Natural Science Foundation of China (no. 41872245).

Data Availability Statement: Not applicable.

Conflicts of Interest: The authors declare no conflict of interest.

References

1. Mallick, K.; Vasanthi, A.; Sharma, K.K. *Bouguer Gravity Regional and Residual Separation: Application to Geology and Environment*; Springer: New York, NY, USA, 2012.
2. Hinze, W.J.; von Frese, R.R.B.; Saad, A.H. *Gravity and Magnetic Exploration: Principles, Practices, and Applications*; Cambridge University Press: New York, NY, USA, 2013.
3. Jacoby, W.; Smilde, P.L. *Gravity Interpretation: Fundamentals and Application of Gravity Inversion and Geological Interpretation*; Springer: Berlin/Heidelberg, Germany, 2009.
4. Naidu, P.S.; Mathew, M.P. *Analysis of Geophysical Potential Fields: A Digital Signal Processing Approach*; Elsevier Science B.V.: Amsterdam, The Netherlands, 1998.
5. Báth, B.M. *Spectral Analysis in Geophysics*; Elsevier Scientific Publishing Company: Amsterdam, The Netherlands, 1982.
6. Buttkus, B. *Spectral Analysis and Filter Theory in Applied Geophysics*; Springer: Berlin/Heidelberg, Germany, 1991.
7. Foufoula-Georgiou, E.; Kumar, P. *Wavelets in Geophysics*; Academic Press: New York, NY, USA, 1994.
8. Lv, P.F.; Wu, X.; Zhao, Y.; Chang, J.H. Noise removal for semi-airborne data using wavelet threshold and singular value decomposition. *J. Appl. Geophys.* **2022**, *201*, 104622. [[CrossRef](#)]
9. Scholz, C.H.; Mandelbrot, B.B. *Fractals in Geophysics*; Springer: Basel, Switzerland, 1989.
10. Turcotte, D.L. *Fractals and Chaos in Geology and Geophysics*; Cambridge University Press: New York, NY, USA, 1997.
11. Dimri, V.P. *Fractal Solutions for Understanding Complex Systems in Earth Sciences*; Springer: New York, NY, USA; Cham, Switzerland; Heidelberg, Germany, 2016.
12. Sankar, G.S.; Dimri, V.P. Interpretation of gravity data using eigenimage with Indian case study: A SVD approach. *J. Appl. Geophys.* **2013**, *95*, 23–35. [[CrossRef](#)]
13. Chen, Y.Q.; Zhang, L.N.; Zhao, B.B. Application of singular value decomposition (SVD) in extraction of gravity components indicating the deeply and shallowly buried granitic complex associated with tin polymetallic mineralization in the Gejiu tin ore field, Southwestern China. *J. Appl. Geophys.* **2015**, *123*, 63–70. [[CrossRef](#)]
14. Beiki, M. TSVD analysis of Euler deconvolution to improve estimating magnetic source parameters: An example from the Asele area, Sweden. *J. Appl. Geophys.* **2013**, *90*, 82–91. [[CrossRef](#)]
15. Wang, G.W.; Zhang, S.T.; Yan, C.H.; Xu, G.Y.; Ma, M.; Li, K.; Feng, Y. Application of the multifractal singular value decomposition for delineating geophysical anomalies associated with molybdenum occurrences in the Luanchuan ore field (China). *J. Appl. Geophys.* **2012**, *86*, 109–119. [[CrossRef](#)]
16. Zhao, B.B.; Chen, Y.Q. Singular value decomposition (SVD) for extraction of gravity anomaly associated with gold mineralization in Tongshi gold field, Western Shandong Uplifted Block, Eastern China. *Nonlinear Proc. Geophys.* **2011**, *18*, 103–109. [[CrossRef](#)]
17. Huang, N.E.; Wu, Z.H. A review on Hilbert-Huang transform: Method and its applications to geophysical studies. *Rev. Geophys.* **2008**, *46*, RG2006. [[CrossRef](#)]
18. Huang, N.E.; Shen, Z.; Long, S.R.; Wu, M.C.; Shih, H.H.; Zheng, Q.; Yen, N.-C.; Tung, C.C.; Liu, H.H. The empirical mode decomposition and the Hilbert spectrum for nonlinear and non-stationary time series analysis. *Proc. R. Soc. Lond. A* **1998**, *454*, 903–995. [[CrossRef](#)]
19. Xu, G.M.; Cheng, Q.M. Comparing BEMD and BEEMD for identifying geochemical anomalies associated with Cu polymetallic mineralization in the southwestern Fujian province (China). *Geochemistry* **2022**, *82*, 125905. [[CrossRef](#)]
20. Xu, G.M.; Cheng, Q.M.; Zuo, R.G.; Wang, H.C. Application of improved bi-dimensional empirical mode decomposition (BEMD) based on Perona-Malik to identify copper anomaly association in the southwestern Fujian (China). *J. Geochem. Explor.* **2016**, *164*, 65–74. [[CrossRef](#)]
21. Battista, B.M.; Knapp, C.; McGee, T.; Goebel, V. Application of the empirical mode decomposition and Hilbert-Huang transform to seismic reflection data. *Geophysics* **2007**, *72*, H29–H37. [[CrossRef](#)]
22. Chen, Y.K.; Zhang, G.Y.; Gan, S.W.; Zhang, C.L. Enhancing seismic reflections using empirical mode decomposition in the flattened domain. *Appl. Geophys.* **2015**, *119*, 99–105. [[CrossRef](#)]
23. Shaw, P.K.; Saha, D.; Ghosh, S.; Janaki, M.S.; Iyengar, A.N.S. Investigation of coherent modes in the chaotic time series using empirical mode decomposition and discrete wavelet transform analysis. *Chaos Soliton Fract.* **2015**, *78*, 285–296. [[CrossRef](#)]
24. Chen, C.; Zhu, X.; Chen, Y.Q.; Zhang, S.T.; Zhao, P.D. Application of BEMD in extraction of magnetic anomaly components associated with Sn-W polymetallic mineralization in SE Yunnan, SW China. *J. Earth Sci.* **2021**, *32*, 318–326. [[CrossRef](#)]

25. Shang, Z.; Chen, Y.Q.; Xu, X.T.; Zhao, B.B. Extraction of gravity—Magnetic anomalies associated with Pb–Zn–Fe polymetallic mineralization in Luziyuan ore field, Yunnan Province, Southwestern China. *Nat. Resour. Res.* **2021**, *31*, 1963–1979. [\[CrossRef\]](#)
26. Huang, J.N.; Zhao, B.B.; Chen, Y.Q.; Zhao, P.D. Bidimensional empirical mode decomposition (BEMD) for extraction of gravity anomalies associated with gold mineralization in the Tongshi gold field, Western Shandong Uplifted Block, Eastern China. *Comput. Geosci.* **2010**, *36*, 987–995. [\[CrossRef\]](#)
27. Chen, J.G.; Xiao, F.; Chang, T. Gravity and magnetic anomaly separation based on bidimensional empirical mode decomposition. *J. Earth Sci.* **2011**, *36*, 327–335. (In Chinese with English Abstract)
28. Hou, W.S.; Yang, Z.J.; Zhou, Y.Z.; Zhang, L.P.; Wu, W.L. Extracting magnetic anomalies based on an improved BEMD method: A case study in the Pangxidong Area, South China. *Comput. Geosci.* **2012**, *48*, 1–8. [\[CrossRef\]](#)
29. Zhao, J.; Zhao, P.D.; Chen, Y.Q. Using an improved BEMD method to analyse the characteristic scale of aeromagnetic data in the Gejiu region of Yunnan, China. *Comput. Geosci.* **2016**, *88*, 132–141. [\[CrossRef\]](#)
30. Chen, Y.Q.; Zhang, L.N.; Zhao, B.B. Application of Bi-dimensional empirical mode decomposition (BEMD) modeling for extracting gravity anomaly indicating the ore-controlling geological architectures and granites in the Gejiu tin-copper polymetallic ore field, southwestern China. *Ore Geol. Rev.* **2017**, *88*, 832–840. [\[CrossRef\]](#)
31. Asl, A.A.; Manaman, N.S. Locating magnetic sources by empirical mode decomposition. *J. Appl. Geophys.* **2018**, *159*, 329–340. [\[CrossRef\]](#)
32. Mandal, A.; Niyogi, S. Filter assisted bi-dimensional empirical mode decomposition: A hybrid approach for regional-residual separation of gravity anomaly. *J. Appl. Geophys.* **2018**, *159*, 218–227. [\[CrossRef\]](#)
33. Kim, D.; Kim, K.O.; Oh, H.S. Extending the scope of empirical mode decomposition by smoothing. *EURASIP J. Adv. Sig. Pr.* **2012**, *168*, 1–17. [\[CrossRef\]](#)
34. Kim, D.; Park, M.; Oh, H.S. Bidimensional statistical empirical mode decomposition. *IEEE Signal Proc. Lett.* **2012**, *19*, 191–194. [\[CrossRef\]](#)
35. Yadav, I.C.; Shah Nawazuddin, S.; Pradhan, G. Addressing noise and pitch sensitivity of speech recognition system through variational mode decomposition based spectral smoothing. *Digit. Signal Process.* **2019**, *86*, 55–64. [\[CrossRef\]](#)
36. Wu, Z.H.; Huang, N.E. Ensemble empirical mode decomposition: A noise-assisted data analysis method. *Adv. Data Sci. Adapt. Anal.* **2009**, *1*, 1–41. [\[CrossRef\]](#)
37. Park, M.; Kim, D.; Oh, H.S. Quantile-based empirical mode decomposition: An efficient way to decompose noisy signals. *IEEE Trans. Instrum. Meas.* **2015**, *64*, 1802–1813. [\[CrossRef\]](#)
38. Ali, M.; Khan, D.M.; Alshanbari, H.M.M.; El-Bagoury, A.A.A.H. Prediction of complex stock market data using an improved hybrid EMD-LSTM model. *Appl. Sci.* **2023**, *13*, 1429. [\[CrossRef\]](#)
39. Jaber, A.M.; Ismail, M.T. Trend extraction using empirical mode decomposition and statistical empirical mode decomposition: Case study: Kuala Lumpur stock market. *AIP Conf. Proc.* **2014**, *1635*, 776–779. [\[CrossRef\]](#)
40. Biswas, M.; Dey, D. Bi-dimensional statistical empirical mode decomposition-based video analysis for detecting colon polyps using composite similarity measure. In Proceedings of the 1st International Conference on Intelligent Computing, Communication and Devices (ICCD), SOA University, Bhubaneswar, India, 18–19 April 2014; pp. 297–308.
41. Santisteban, J.I.; Mediavilla, R.; Celis, A.; Castano, S.; de la Losa, A. Millennial-scale cycles of aridity as a driver of human occupancy in central Spain? *Quatern. Int.* **2016**, *407*, 96–109. [\[CrossRef\]](#)
42. Huang, B.Q.; Kunoth, A. An optimization based empirical mode decomposition scheme. *J. Comput. Appl. Math.* **2013**, *240*, 174–183. [\[CrossRef\]](#)
43. Arfia, F.B.; Sabri, A.; Messaoud, M.B.; Sabri, A. Choosing interpolation RBF function in image filtering with the bidimensional empirical modal decomposition. In Proceedings of the 1st International Conference on Advanced Technologies for Signal and Image Processing (ATSIP), Sousse, Tunisia, 17–19 March 2014; pp. 361–366.
44. Jia, L.S.; Zhang, Q.; Zheng, X.; Yao, P.L.; He, X.G.; Wei, X.H. The empirical optimal envelope and its application to local mean decomposition. *Digit. Signal Process.* **2019**, *87*, 166–177. [\[CrossRef\]](#)
45. Hastie, T.; Tibshirani, R.; Friedman, J. *The Elements of Statistical Learning: Data Mining, Inference, and Prediction*; Springer: New York, NY, USA, 2009.
46. Ghosh, S. *Kernel Smoothing: Principles, Methods and Applications*; John Wiley & Sons, Inc.: Hoboken, NJ, USA, 2018.
47. Fan, J.Q.; Gijbels, I. Data-driven bandwidth selection in local polynomial fitting: Variable bandwidth and spatial adaptation. *J. R. Stat. Soc. B* **1995**, *57*, 371–394. [\[CrossRef\]](#)
48. Fan, J.Q.; Gijbels, I. *Local Polynomial Modelling and Its Applications*; CRC Press: Boca Raton, FL, USA, 1996.
49. Xiao, W.J.; Zhang, L.C.; Qin, K.Z.; Sun, S.; Li, J.L. Paleozoic accretionary and collisional tectonics of the Eastern Tianshan (China): Implications for the continental growth of Central Asia. *Am. J. Sci.* **2004**, *304*, 370–395. [\[CrossRef\]](#)
50. Xiao, F.; Wang, Z.H. Geological interpretation of Bouguer gravity and aeromagnetic data from the Gobi-desert covered area, Eastern Tianshan, China: Implications for porphyry Cu–Mo polymetallic deposits exploration. *Ore Geol. Rev.* **2017**, *80*, 1042–1055. [\[CrossRef\]](#)
51. Xiao, F.; Wang, K.Q.; Hou, W.S.; Wang, Z.H.; Zhou, Y.Z. Prospectivity mapping for porphyry Cu–Mo mineralization in the eastern Tianshan, Xinjiang, northwestern China. *Nat. Resour. Res.* **2020**, *29*, 89–113. [\[CrossRef\]](#)
52. Xiao, F.; Chen, W.L.; Wang, J.; Erten, O. A hybrid logistic regression: Gene expression programming model and its application to mineral prospectivity mapping. *Nat. Resour. Res.* **2021**, *31*, 2041–2064. [\[CrossRef\]](#)

53. Wang, Y.F.; Chen, H.Y.; Falloon, T.J.; Han, J.S. The Paleozoic-Mesozoic magmatic evolution of the Eastern Tianshan, NW China: Constraints from geochronology and geochemistry of the Sanchakou intrusive complex. *Gondwana Res.* **2022**, *103*, 1–22. [[CrossRef](#)]
54. Wang, Z.G.; Zhu, X.Q.; Bi, H.; Wang, Y.L.; Wu, B.Q.; Zou, T.R.; Zhao, Z.H.; Gui, X.T. *Granites in Xinjiang, China*; Geological Publishing House: Beijing, China, 2006. (In Chinese with English Abstract)
55. Chen, Y.C.; Liu, D.Q.; Tang, Y.L.; Wang, D.H.; Dong, L.H.; Xu, X.; Wang, X.D. *Mineral Resources and Mineralization System in Tianshan, China*; Geological Publishing House: Beijing, China, 2008. (In Chinese with English Abstract)
56. Zhang, L.C.; Liu, D.Q.; Wang, Y.B.; Li, Q.C.; Li, B.Q. *Metallogenic Rules of Dominant Metal Minerals in Xinjiang, China*; Geological Publishing House: Beijing, China, 2006. (In Chinese with English Abstract)
57. Xiao, F.; Chen, J.G.; Agterberg, F.P.; Wang, C.B. Element behavior analysis and its implications for geochemical anomaly identification: A case study for porphyry Cu-Mo deposits in Eastern Tianshan, China. *J. Geochem. Explor.* **2014**, *145*, 1–11. [[CrossRef](#)]
58. Liu, D.Q.; Tang, Y.L.; Zhou, R.H. *Copper Deposits and Nickle Deposits in Xinjiang, China*; Geological Publishing House: Beijing, China, 2005.
59. Wu, G.G.; Dong, L.H.; Xue, C.J. *The Main Porphyry Copper Ore Belts in the North Xinjiang, China*; Geological Publishing House: Beijing, China, 2008.
60. Shao, X.L. Research for Geophysical Characteristics and Prospecting Application on Huangshan-Jingerquan Ultramafic Complex Belt in Eastern Tianshan of Xinjiang. Ph.D. Thesis, China University of Geosciences, Beijing, China, 2012.
61. Zhuang, D.Z. Research on Metallogenic Geological Conditions and the Predicting Models of Compound Information in East Tianshan of Xinjiang. Ph.D. Thesis, Jilin University, Changchun, China, 2005.

Disclaimer/Publisher's Note: The statements, opinions and data contained in all publications are solely those of the individual author(s) and contributor(s) and not of MDPI and/or the editor(s). MDPI and/or the editor(s) disclaim responsibility for any injury to people or property resulting from any ideas, methods, instructions or products referred to in the content.